

CrossMark
click for updatesCite this: *RSC Adv.*, 2014, 4, 51286

Synthesis and characterization of platinum modified TiO₂-embedded carbon nanofibers for solar hydrogen generation†

Minju Kim,‡^a Abdul Razzaq,‡^a Young Kwang Kim,^b Soonhyun Kim*^b and Su-Il In*^a

Photocatalytic water splitting is a significant and promising technology to generate hydrogen, an alternative and clean future fuel. The present work describes the preparation and application of a TiO₂ based photocatalyst with an effective architecture focused on the key issues of photocatalyst reusability and photocatalytically stable activity. TiO₂ nanoparticles were embedded onto carbon nanofibers (CNF) acting as a support. The electrospinning method was adopted for fabrication of TiO₂ embedded carbon nanofibers (TiO₂/CNF). The photocatalytic activity of the TiO₂/CNF under simulated light was improved by Pt co-catalyst photodeposition. The morphological and structural properties of TiO₂/CNF and Pt photodeposited TiO₂/CNF (Pt-TiO₂/CNF) were investigated by field emission scanning electron microscopy (FESEM), high resolution transmission electron microscopy (HRTEM) and powder X-ray diffraction (XRD) techniques. The surface characteristics of these materials were investigated by X-ray photoelectron spectroscopy (XPS), photocurrent and photoluminescence (PL) measurements were also used to elaborate the effect of Pt photodeposition. The reusability and photocatalytic stability of Pt-TiO₂/CNF was tested by the generation of approximately the same amounts of photocatalytic hydrogen with the same sample under the same conditions of illumination. The highest production rate of photocatalytic hydrogen generation achieved under simulated light was 3.5 μmol (after 3 hours of illumination with 0.02 g of photocatalyst). These tests show that Pt-TiO₂/CNF is a reusable photocatalyst with a promising stable photocatalytic performance for solar energy conversion applications.

Received 10th August 2014
Accepted 2nd October 2014

DOI: 10.1039/c4ra08455a

www.rsc.org/advances

1. Introduction

Hydrogen has emerged as a potential energy carrier in various low greenhouse gas energy applications due to its renewability and neutral impact on the environment. Hydrogen can be produced by various methods such as (i) steam reforming of natural gas,¹ (ii) biomass reforming,² (iii) water electrolysis,³ (iv) photocatalytic water splitting⁴ and (v) photoelectrochemical water splitting.⁵ Currently, a major part of hydrogen used for industrial and commercial applications is being produced from fossil fuels. The limited reserves and pollutant emissions from fossil fuels have been directing the research efforts to focus on

alternative renewable approaches for meeting hydrogen demand. The pioneering work of solar hydrogen evolution by Fujishima and Honda opened a new path to global research for clean and eco-friendly solar hydrogen production.⁵ A tremendous amount of research has been conducted for the development of efficient photocatalytic systems to produce hydrogen either by photoelectrochemical or photocatalytic water splitting. Despite of extensive research, photocatalytic water splitting still requires massive efforts to increase the yield of hydrogen with stable performance before it will be a competitive and a cost effective technology. The key aspect of photocatalytic water splitting is the use of photocatalysts, which create electron-hole pairs upon sunlight absorption. The electrons thus created can reduce hydrogen ions (H⁺) generated by water splitting into hydrogen. There are numerous methods for improving the photocatalytic hydrogen yield, which include designing novel photocatalysts,⁶ co-catalyst loading,⁷ using mixed semiconductors,⁸ modification with non-metals such as nitrogen,⁹ and carbon,¹⁰ Z-schemes mechanism¹¹ and by the addition of hole scavengers.¹² Most of the above mentioned methods employ powder photocatalysts dispersed in water for photocatalytic hydrogen generation. The powder photocatalysts bear the advantages of well dispersion and large scale applications. However, a major disadvantage is inadequate recovery or

^aDepartment of Energy Systems Engineering, Daegu Gyeongbuk Institute of Science and Technology (DGIST), 50-1 sang ri, Hyeon-pung myun, Dalseong Gun, Daegu, Republic of Korea. E-mail: insuil@dgist.ac.kr; Fax: +82-53-785-6409; Tel: +82-53-785-6417

^bNano & Bio Research Division, Daegu Gyeongbuk Institute of Science and Technology (DGIST), 50-1 sang ri, Hyeon-pung myun, Dalseong Gun, Daegu, Republic of Korea. E-mail: sh2358@dgist.ac.kr; Fax: +82-53-785-6409; Tel: +82-53-785-6417

† Electronic supplementary information (ESI) available: Additional XRD, XPS, photocatalytic hydrogen generation plot, Pt atomic concentration table, photocurrent profiles, and photoluminescence spectra. See DOI: 10.1039/c4ra08455a

‡ Both authors contributed equally to this work.

separation of powder photocatalyst from the photoreactor after photocatalytic reactions leading to the issues of reusability and stable photocatalytic performance. Moreover, the aggregation of powder photocatalysts¹³ and influence on the physical properties of the materials during photoirradiation¹⁴ limit the use of powder photocatalysts.

To overcome the critical issue of reusability for spent nanostructured photocatalysts, the nanofibrous morphology of photocatalyst seems to be an attractive and effective strategy.^{15,16} Several researchers have been investigating various approaches for synthesis of photocatalyst nanofibers (NF) such as doped photocatalyst NF,^{17,18} cocatalyst loaded photocatalyst NF,¹⁹ heterojunction photocatalyst NF²⁰ and photocatalyst nanoparticles (NP) embedded inorganic or polymer NF.^{21–23} In the latest approach, NF acts as structural support for embedded photocatalyst NP, increasing their reusability, thermal and chemical stability. In this regard, Fan *et al.*²¹ investigated the successful growth of ZnIn₂S₄ and ZnS–AgIn₂S₈ NP on electrospun fluoropolymer nanofibers, achieving much enhanced photocatalytic hydrogen generation. The fluoropolymer support also demonstrated excellent stability in thermal, radiational and chemical treatment. Tong *et al.*²² reported electrospun PAN/Ag/Pd composite NF with improved photocatalytic hydrogen generation. This material also shows excellent recycling stability. In addition to the polymeric supporting materials, carbon nanofibers (CNF) have also attracted a wider attention as a support material due to their unique properties and broader application range.^{24,25} The numerous advantages possessed by CNF include high surface area,²⁶ potential as a candidate for hydrogen storage,²⁷ efficient catalytic supports²⁸ and possible super capacitor applications in the near future.²⁹ Furthermore, it is well known that the photocatalytic efficiency can be improved by coupling with carbon nanomaterials due to enhanced charge separation efficiency.³⁰

In this paper, a mixed phase (anatase and rutile) TiO₂ nanoparticles embedded carbon nanofibers (TiO₂/CNF) were fabricated with the following objectives: (i) preparation of TiO₂/CNF photocatalyst for easy recovery and reusability of spent photocatalyst and (ii) to attain a stable photocatalytic performance of recovered TiO₂/CNF photocatalyst. Furthermore, the photocatalytic property of TiO₂/CNF was modified by Pt deposition. The fabricated material was evaluated by the photocatalytic hydrogen generation. To the best of our knowledge there is no report regarding the application of TiO₂ nanoparticles embedded carbon nanofibers (TiO₂/CNF) in photocatalytic hydrogen generation. The TiO₂ nanoparticles were encapsulated with CNF to avoid the inadequate recovery loss of TiO₂ photocatalyst in the process of photocatalytic hydrogen generation. TiO₂/CNF were synthesized by carbothermal reaction of TiO₂ embedded polyacrylonitrile (TiO₂/PAN).³¹ The TiO₂/PAN nanofibers were harvested by electrospinning technique.^{32,33} The electrospinning method is considered to be simple and versatile technique for producing ultra-fine thin nanofibers. Pt was photodeposited with varied deposition times on the TiO₂/CNF surface. The photodeposition method employed here is considered as a comparatively economical method to other deposition methods.^{34,35} Photocatalytic

hydrogen was generated by employing Pt–TiO₂/CNF under simulated solar irradiation at ambient temperature. Methanol, acting as a hole scavenger, was added to the water. The photocatalytic stability test for Pt–TiO₂/CNF was demonstrated by generation of similar amounts of photocatalytic hydrogen under the same experimental conditions with same recovered material, ensuring our strategy to be a promising and effective approach addressing specifically the reusability and photocatalytic stability of photocatalyst.

2. Experimental

2.1. Materials and reagents

Commercially available TiO₂ P25 (Degussa), polyacrylonitrile, (PAN, 99.0%, Aldrich), *N,N*-dimethylformamide (DMF, 99.0%, Samchun chemicals), Methanol (100.0%, J. T. Braker) and hydrogen hexachloroplatinate (IV) hydrate (H₂PtCl₆·6H₂O, Kojima chemicals) were used as received. Deionized water (resistivity >18 μm) was used throughout the experiments.

2.2. Preparation of TiO₂/CNF

A solution of PAN in DMF (10.0 wt%) was first prepared in a beaker under magnetic stirring. The stirring was performed at a temperature of 60 °C and continued for 96 hours to achieve a homogeneous solution. TiO₂ P25 powder (1.0 g) was dispersed under stirring in this homogeneous solution (10.0 g). The stirring was continued for 3 days followed by a mild sonication at ambient conditions, resulting in a well dispersed yellowish TiO₂/PAN gel. The TiO₂/PAN nanofibers were fabricated using TiO₂/PAN gel *via* electrospinning technique. The details of the electrospinning technique are described in previous work.²⁶ A dense web of TiO₂/PAN nanofibers was carbonized in a tube furnace under nitrogen streaming to produce titanium carbonitride embedded CNF (TiCN/CNF). The carbonization process consisted of the following steps: (i) stabilization of TiO₂/PAN nanofibers in air at a temperature of 250 °C for 20 minutes followed by (ii) carbonization of TiO₂/PAN nanofibers at 750 °C for 1 hour and (iii) finally heating the TiO₂/PAN nanofibers at 1400 °C for 1 hour. Both, carbonization and final heating steps were carried out under N₂ streaming. During carbonization process a ramp rate of 5 °C min⁻¹ was applied between all plateaus of 250 °C, 750 °C and 1400 °C. Further oxidation of TiCN/CNF was carried out for its conversion to TiO₂/CNF at 410 °C for 90 minutes with a ramp rate of 5 °C min⁻¹ in the furnace. The schematic presenting the synthesis of TiO₂/CNF is shown in Fig. 1.

2.3. Preparation of Pt–TiO₂/CNF

To improve the photocatalytic activity of TiO₂/CNF, Pt cocatalyst was deposited on the surface of TiO₂/CNF *via* photodeposition method.^{34,35} Pt photodeposition was conducted in a quartz reactor (7.5 ml) containing an aqueous solution (5.0 ml) of H₂PtCl₆·6H₂O (0.15 mmol) and methanol (10.0 vol%) as a sacrificial hole scavenger. TiO₂/CNF (0.02 g) was added into the quartz reactor and different amounts of Pt were photodeposited on its surface. Any air present inside the quartz reactor was

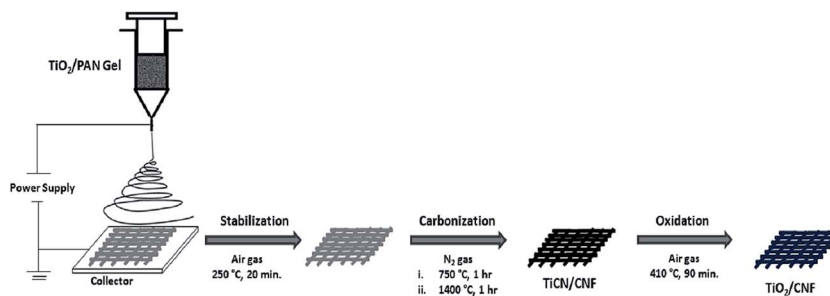


Fig. 1 Schematic representation of TiO_2/CNF fabrication.

removed prior to photodeposition experiments by N_2 gas streaming for 30 minutes. A 300 W Xe arc lamp (Oriel) with a 10.0 cm long IR water filter and a UV cutoff filter ($\lambda > 295$ nm) was used as a light source for Pt photodeposition. Various samples of Pt photodeposited TiO_2/CNF ($\text{Pt}(n)\text{-TiO}_2/\text{CNF}$, where $n = \text{Pt photodeposition time}$) were prepared by varying Pt photodeposition time as 0, 30, 60, 120 and 180 minutes. All the $\text{Pt}(n)\text{-TiO}_2/\text{CNF}$ samples prepared were thoroughly cleaned with DI water and dried under ambient conditions for 24 hours. The samples obtained after drying were labeled as $\text{Pt}(0)\text{-TiO}_2/\text{CNF}$, $\text{Pt}(30)\text{-TiO}_2/\text{CNF}$, $\text{Pt}(60)\text{-TiO}_2/\text{CNF}$, $\text{Pt}(120)\text{-TiO}_2/\text{CNF}$ and $\text{Pt}(180)\text{-TiO}_2/\text{CNF}$ corresponding to their respective Pt photodeposition times.

2.4. Photocatalytic hydrogen generation

The photocatalytic hydrogen generation was demonstrated in a Quartz reactor (7.5 ml). A specific amount of $\text{Pt-TiO}_2/\text{CNF}$ photocatalyst (4.0 g L^{-1}) was placed in a solution of H_2O (5.0 ml) and methanol (0.5 ml). Any air present was purged by N_2 streaming for 30 minutes prior to photoirradiation. The reactor was illuminated for 3 hours using light from a 300 W Xe arc lamp (Oriel) after passing through a 10.0 cm long IR water filter and a UV cutoff filter ($\lambda > 295$ nm). The photocatalytic hydrogen generation was studied with batch system using bare TiO_2/CNF and $\text{Pt}(n)\text{-TiO}_2/\text{CNF}$ samples. The amount of hydrogen produced was monitored at 30 minute intervals by gas chromatography (GC, HP 6890) equipped with a Molsieve column and a thermal conductivity detector (TCD). The reusability and photocatalytic stability tests were conducted using the $\text{Pt}(120)\text{-TiO}_2/\text{CNF}$ sample. The sample was withdrawn from the photo-reactor after first cycle (3 hours illumination) and was retested for additional four cycles of photocatalytic hydrogen generation under the same experimental conditions.

2.5. Photocurrent and photoluminescence measurements

Photocurrent and photoluminescence measurements were taken for CNF, TiCN/CNF , TiO_2/CNF and $\text{Pt-TiO}_2/\text{CNF}$. The photocurrent was measured using three-electrode system in a 0.1 M Na_2SO_4 buffer (\sim neutral pH). The working electrode size was fixed at $1 \text{ cm} \times 3 \text{ cm}$. The reference electrode and counter electrode were Ag/AgCl and Pt wire, respectively. N_2 was continuously purged before and during photocurrent measurement, and a constant potential (0.5 V vs. Ag/AgCl) was

applied to the working electrode using a potentiostat (VSP, Princeton Applied Research). Photocurrent generations were measured under AM 1.5 light irradiation (Abet technology). Mixed solution was stirred for 100 seconds for stabilization. Then light was irradiated for 100 seconds and light off for 100 seconds.

Photoluminescence (PL) experiments were performed with a spectrometer ($f = 0.5 \text{ m}$, Acton Research Co., Spectrograph 500i), and an intensified photo diode array detector (Princeton Instrument Co., IRY1024) equipped with 325 nm He-Cd laser (Kimon, 1 K, 50 mW).

2.6. Characterization of $\text{Pt-TiO}_2/\text{CNF}$

The morphological analysis of TiO_2/PAN nanofibers, TiCN/CNF , and TiO_2/CNF were done using a field emission scanning electron microscope (FESEM, Hitachi S-4800). Powder X-ray diffraction (XRD) patterns of the samples were recorded in a wide angle range ($2\theta = 20\text{--}80^\circ$) using an X-ray diffractometer (Panalytical, Empyrean) operating at 40 kV and 30 mA with $\text{Cu K}\alpha$ radiation ($\lambda = 1.54187 \text{ \AA}$). The transmission electron microscopy (TEM) and the selected area electron diffraction (SAED) patterns of $\text{Pt}(180)\text{-TiO}_2/\text{CNF}$ were obtained using a field emission transmission electron microscope (FETEM, Hitachi HF-3300) instrument operating at 300 kV. The surface composition, their oxidation states, and atomic ratios of the samples were determined by X-ray photoelectron spectroscopy (XPS, Thermo VG, K-alpha) using Al $\text{K}\alpha$ line (148 606 eV) as the X-ray source.

3. Results and discussion

3.1. Morphological properties of TiO_2/CNF

FESEM images of TiO_2/PAN nanofibers, TiCN/CNF and TiO_2/CNF are shown in Fig. 2. Fig. 2a shows a dense web of well aligned TiO_2/PAN nanofibers (diameter = 550 nm) as synthesized. After carbonization of TiO_2/PAN , a decrease in the thickness of TiCN/CNF (390 nm) was noticed (Fig. 2b). The formation of carbon from PAN at high temperature caused shrinkage of the TiO_2/PAN nanofibers.³⁶ However, no significant change in the morphology of TiO_2/CNF (Fig. 2c) was observed after the oxidation of TiCN/CNF . The FESEM image of a selected TiO_2/CNF is shown in Fig. 2d. The image clearly displays random embedment of TiO_2 nanoparticles on the CNF surface.

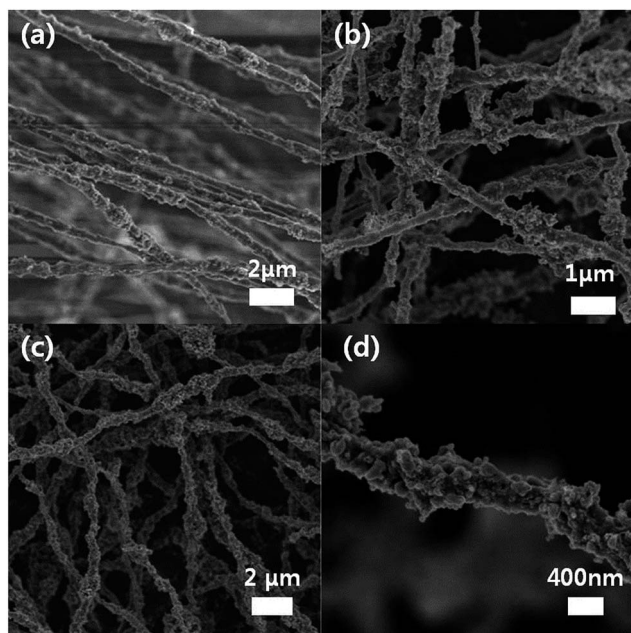


Fig. 2 FESEM images of (a) TiO_2/PAN nanofibers, (b) TiCN/CNF , (c) TiO_2/CNF and (d) a selected TiO_2/CNF exposing the embedment of TiO_2 nanoparticles.

3.2. XRD analysis

Fig. 3 shows XRD patterns of TiO_2/PAN , TiCN/CNF and TiO_2/CNF . TiO_2/PAN consists of highly crystalline anatase (A) co-existing with small amounts of rutile (R) TiO_2 phase (Fig. 3a). The sample exhibits main diffraction peaks of anatase and rutile phases of TiO_2 at 2θ values of 25.2° and 27.5° respectively along with other respective minor peaks.¹⁰ After the carbonization process, the peaks of anatase and rutile phases of TiO_2 disappear with the appearance of various other diffraction peaks at 2θ values of 36° , 42.7° , 62° , 74° , and 78° (Fig. 3b). These diffraction peaks are attributed to the formation of Titanium carbide (TC) in CNF,^{37–39} ensuring the formation of TiCN/CNF as an intermediate product. However, after oxidation of $\text{TiCN}/$

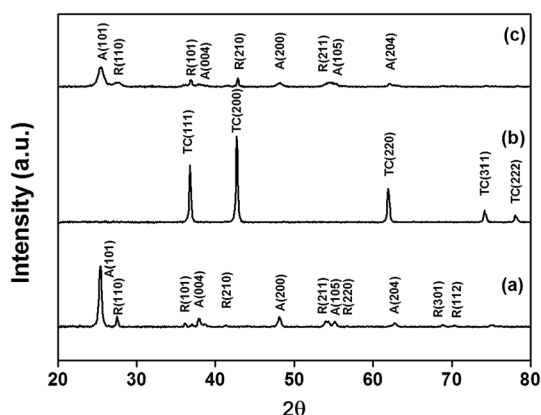


Fig. 3 XRD patterns of (a) TiO_2/PAN , (b) TiCN/CNF and (c) TiO_2/CNF (A, anatase; R, rutile; TC, titanium carbide).

CNF , the main peaks of anatase and rutile TiO_2 phases reappear in the TiO_2/CNF sample (Fig. 3c). The reappearance of anatase and rutile phases of TiO_2 is accredited to the oxidation of TiCN/CNF during the calcination process.^{31,40,41}

The XRD pattern of $\text{Pt}(n)\text{-TiO}_2/\text{CNF}$ samples ($n = 0, 30, 60, 120$ and 180 minutes of Pt photodeposition) are shown in Fig. S1.† It is obvious that all of the samples show peaks of anatase (A) and rutile (R) phases of TiO_2 in their respective XRD patterns, confirming the presence of TiO_2 . However, it is hard to observe the Pt peaks in the XRD pattern due to the high dispersion of Pt nanoparticles or due to the low level of photodeposition.⁴² Hence, further analyses were conducted to confirm the presence of Pt in these samples and are discussed later.

3.3. TEM studies

Fig. 4a shows a TEM image of a selected $\text{Pt}(180)\text{-TiO}_2/\text{CNF}$. The TEM image reveals the presence of agglomerated nanoparticles on the nanofiber surface. The agglomerated nanoparticles were classified as embedded TiO_2 and photodeposited Pt nanoparticles by scanning transmission electron microscopy (STEM) analysis. The STEM image (Fig. 4b) illustrates randomly distributed brighter and darker regions on the nanofiber surface. The brighter regions are attributed to photodeposited Pt nanoparticles, whereas the darker regions indicate the embedment of TiO_2 nanoparticles.⁴³ The randomness of the brighter regions, as indicated by dotted circles, points to varying amounts of Pt photodeposition on the nanofiber surface. The High resolution transmission electron microscopy (HRTEM) image (Fig. 4c) of brighter region observed by STEM was taken to investigate the interface region between Pt and TiO_2 . It can be

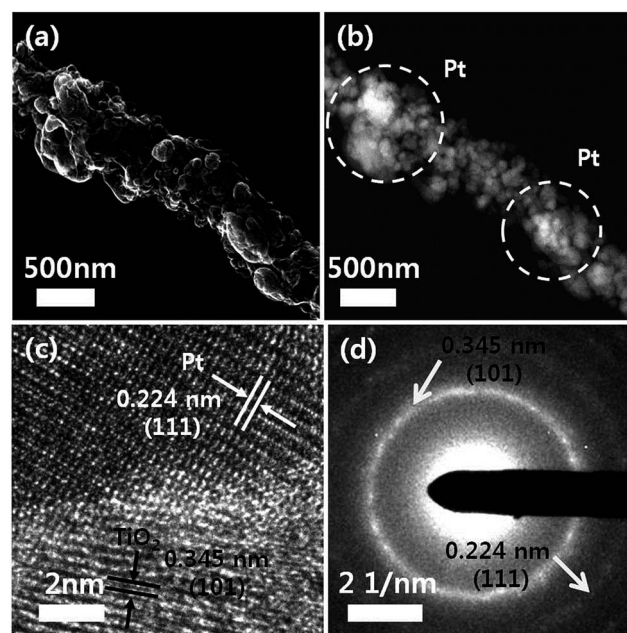


Fig. 4 Representative images of $\text{Pt}(180)\text{-TiO}_2/\text{CNF}$: (a) TEM image of a selected nanofiber, (b) STEM image of (a), (c) HRTEM image and (d) SAED pattern.

seen that the HRTEM of brighter region for representative Pt(180)-TiO₂/CNF displays well defined interface and lattice fringes of Pt and TiO₂. The interface between Pt and TiO₂, as shown by HRTEM image also supports the successful photodeposition of Pt on the TiO₂ nanoparticles. A lattice spacing of 0.345 nm is associated to the *d*₁₀₁ plane of anatase TiO₂ (ref. 44) and 0.224 nm corresponds to the *d*₁₁₁ plane of cubic Pt.⁴⁵ In addition, the selected area electron diffraction (SAED) pattern of the Pt-TiO₂ interface, observed in HRTEM (Fig. 4c) was studied. Fig. 4d shows the SAED patterns of Pt(180)-TiO₂/CNF, which clearly demonstrates the polycrystalline nature of the selected area. The diffraction pattern shows rings which can be indexed to the *d*₁₀₁ plane of anatase TiO₂ and the *d*₁₁₁ plane of Pt.

3.4. XPS studies

X-ray photoelectron spectroscopy (XPS) analysis of the representative Pt(180)-TiO₂/CNF was conducted to investigate the chemical compositions of the photocatalyst. Furthermore, XPS data provides additional information regarding the surface composition and binding interaction of different charged species present in Pt(180)-TiO₂/CNF. The complete survey scan of Pt(180)-TiO₂/CNF (Fig. S2†) revealed that the sample surface is mainly composed of titanium, oxygen, platinum and carbon. Fig. 5a-d shows the high resolution XPS spectra of Ti 2p, O 1s, Pt 4f and C 1s regions respectively. The high resolution peaks were deconvoluted to analyze the binding energy signals corresponding to titanium, oxygen, platinum and carbon atoms.

The Ti 2p region (Fig. 5a) shows peaks at 459.3 eV, 460.8 eV, and 465.8 eV. The peaks appearing at 459.3 eV and 465.8 eV can be assigned to Ti 2p_{3/2} and Ti 2p_{1/2} of TiO₂,⁴⁶ verifying the presence of TiO₂ in respective Pt(180)-TiO₂/CNF. Whereas, the peak appearing at 460.8 eV corresponds to the Ti-C bond confirming the embedment of TiO₂ in the CNF *via* Ti-C linkage.⁴⁷ Fig. 5b shows XPS spectra of O 1s region displaying peaks near

530.7 eV and 532.0 eV. Previous studies have attributed the peak at 530.7 eV to Ti-O bond (associated with lattice oxygen of the bulk TiO₂) and the shoulder peak near the binding energy at 532.0 eV to O-C bonds on the surface of TiO₂.⁴⁰ The XPS spectra of the Pt 4f region (Fig. 5c) exhibit peaks at 71.6 eV and 74.9 eV. These peaks can be assigned to Pt 4f_{7/2} due to bulk Pt with an oxidation state of zero (Pt(0)), and Pt 4f_{5/2} associated to the PtO having +4 oxidation (Pt(IV)), assuring the successful photodeposition of Pt on TiO₂/CNF.^{45,48} This indicates that the Pt exhibits in both oxidized state and zero state on TiO₂/CNF providing moderate active sites for photocatalytic hydrogen generation.

Fig. 5d shows the XPS of the C 1s region with peaks appearing at 284.6 eV, 285.7 eV, 286.3 eV, and 288.0 eV. Based on the reported data, these peaks are attributed to C-C, C-O, and C=O, and surface carbonate, respectively.⁴⁹

XPS analysis for the TiCN/CNF and TiO₂/CNF were also conducted to investigate the chemical composition changes after calcination of TiCN/CNF. Fig. S3(a-d)† shows high resolution XPS of Ti 2p, O 1s, C 1s and N 1s for TiCN/CNF and TiO₂/CNF. The Ti 2p region for TiCN/CNF (Fig. S3a†) shows a single peak near 459.3 eV corresponding to Ti 2p_{1/2}. While the Ti 2p region for TiO₂/CNF (Fig. S3a†) exhibits two peaks near 460.0 eV and 465.8 eV corresponding to Ti 2p_{1/2} and Ti 2p_{3/2}, respectively. The shifting of the Ti 2p_{1/2} signal towards a slightly high binding energy and reappearance of the Ti 2p_{3/2} signal in TiO₂/CNF depicts the oxidation of Ti ions present in TiCN/CNF after calcination. Both TiCN/CNF and TiO₂/CNF exhibit a single peak with varied intensity in the O 1s (Fig. S3b†) and the C 1s (Fig. S3c†) regions. The O 1s region shows a peak around 530.7 eV corresponding to the Ti-O bond.⁴⁶ An increase in the intensity of the Ti-O bond signal confirms the reappearance of oxidized Ti states in TiO₂/CNF.⁴⁷ The C 1s region shows a peak associated to C-C bonds appearing near 284.6 eV. A decrease in signal intensities of the C-C bonds observed in TiO₂/CNF reassures the conversion of TiCN to TiO₂ during calcination. Fig. S3d† shows XPS spectra of N 1s regions of TiCN/CNF and TiO₂/CNF. In TiCN/CNF, a strong N 1s signal intensity at 397.1 eV appeared corresponding to Ti-N bonds.⁴⁷ This signal indicates TiN existence on the titanium surface due to accumulation of nitrogen from PAN during the carbothermal reaction. However, after the calcination of TiCN/CNF (carbothermal product) most nitride ions are burned off, resulting in no N 1s signal in TiO₂/CNF. The XPS spectra of Pt(*n*)-TiO₂/CNF samples formed with varied Pt photodeposition times are also shown in Fig. S4.† The atomic ratios for Pt content were calculated using XPS data and is shown in Table S1.† It can be seen that with the increase of Pt photodeposition time, the Pt atomic concentration is increased resulting in the signals intensification of Pt 4f_{7/2}, and Pt 4f_{5/2} irrespective of binding energies. This increase clearly indicates that the increased Pt photodeposition time leads to increase of Pt quantity on the TiO₂/CNF.

3.5. Photocatalytic hydrogen generation

Fig. 6 shows photocatalytic hydrogen generation from different Pt(*n*)-TiO₂/CNF samples. All the samples were irradiated for 3

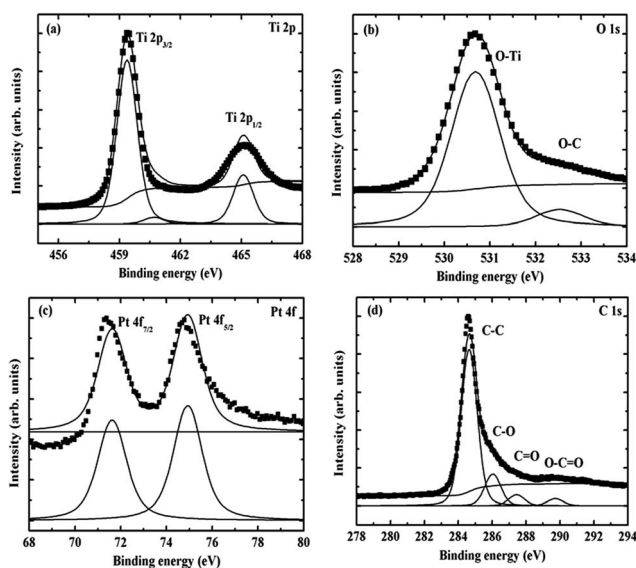


Fig. 5 XPS spectra of Pt(180)-TiO₂/CNF showing the regions of (a) Ti 2p, (b) O 1s, (c) Pt 4f and (d) C 1s.

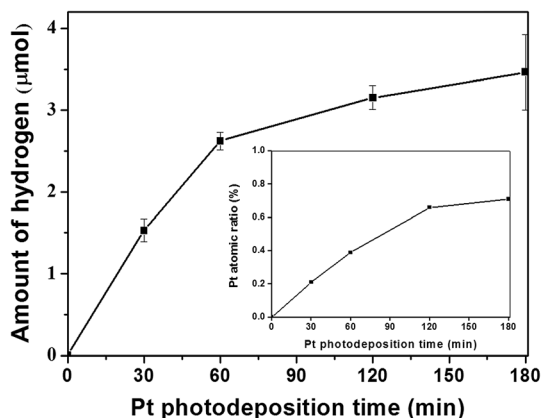


Fig. 6 Amount of photocatalytic hydrogen generated after 3 hours of irradiation employing Pt(*n*)-TiO₂/CNF samples prepared at photodeposition times of 0, 30, 60, 120 and 180 min, respectively. Inset figure shows the relation between Pt atomic ratio with photodeposition times.

hours. It can be seen clearly Pt(*n*)-TiO₂/CNF exhibits a significant enhancement in H₂ evolution as compared to TiO₂/CNF or Pt(0)-TiO₂/CNF sample (without Pt photodeposition) which produces negligible amount of photocatalytic H₂. Thus an increase in photocatalytic performance of Pt(*n*)-TiO₂/CNF is mainly due to photodeposition of Pt nanoparticles. While the beneficial role of CNF remains as a physical support for embedment of TiO₂ nanoparticles contributing to the easy recovery and reusability of photocatalyst. Furthermore increasing the Pt photodeposition times also increased the hydrogen yield. The longer Pt photodeposition time increases the Pt loading, raising the Pt atomic ratio (inset to Fig. 6). The higher Pt atomic ratio results in an increase of electron sinks thus improving the photocatalyst activity with moderate reaction rates.⁴ However, when Pt(*n*)-TiO₂/CNF sample with Pt photodeposition times longer than 120 min was employed, no significant increase in the photocatalytic hydrogen generation was observed. A similar trend was noticed for the Pt atomic ratio with increased Pt photodeposition time (inset to Fig. 6). This may be due to blockage of TiO₂ active sites due to high Pt loading, limiting photocatalytic hydrogen generation.⁵⁰ Due to this converged behavior, experiments for photocatalytic hydrogen generation were bound to the Pt(180)-TiO₂/CNF sample. Thus increase of photocatalytic hydrogen generation for each Pt(*n*)-TiO₂/CNF sample can be attributed to improved photocatalytic activity as a result of Pt photodeposition. The photocatalytic hydrogen generation in all Pt(*n*)-TiO₂/CNF samples increased with longer irradiation time and after 3 hours of irradiation were 0, 1.5, 2.6, 3.2, and 3.5 μmole, respectively (Fig. S5[†]).

It is well known that the deposition of noble metals usually enhance the separation and prolong the lifetime of photo-generated electrons and holes (e⁻-h⁺), resulting in the improved photocatalytic activity.^{51,52} The mechanism involved in the generation of photocatalytic hydrogen employing Pt(*n*)-TiO₂/CNF is illustrated in Fig. 7a. Upon light irradiation, the

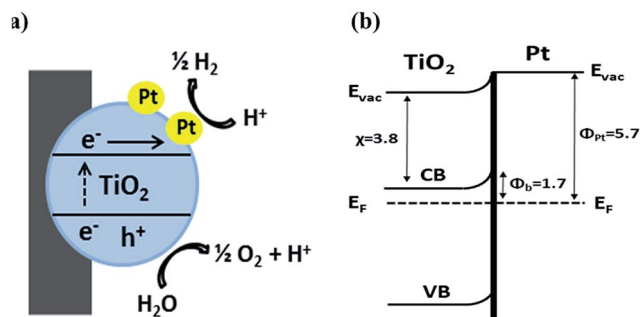


Fig. 7 (a) Schematic illustration of photocatalytic hydrogen generation and (b) energy band diagram for Pt-TiO₂ junction on Pt(*n*)-TiO₂/CNF sample. (E_{vac} , E_F , Φ_{Pt} , χ , Φ_b represents Vacuum level, Fermi level, work function of Pt, electron affinity of TiO₂ conduction band and Schottky barrier height, respectively (all values in eV)).

photogenerated electrons are excited from the valence band to conduction band (CB) of TiO₂ and migrated to Pt nanoparticles which acts as electron traps. On the other hand the holes are accumulated at the TiO₂ valence band (VB). The photogenerated electrons trapped by Pt nanoparticles are transferred to surface adsorbed protons to produce H₂, while the holes diffuse to photocatalyst surface and oxidize water to give oxygen. The Pt nanoparticles photodeposited on TiO₂ result in the formation of Schottky barrier at Pt-TiO₂ interface based on the difference between the Pt work function ($\Phi_{Pt} = 5.7$ eV)⁵³ and the electron affinity ($\chi = 3.8$ eV)⁵⁴ of TiO₂ conduction band (Fig. 7b). The height of Schottky barrier ($\Phi_b = 1.7$ eV)⁵⁵ is appropriate enough for suppressing the e⁻-h⁺ recombination thus acting as an electron trap during the photocatalytic process.

To further support the suppression of the e⁻-h⁺ recombination and improved charge separation by Pt photodeposition, the photocurrent and photoluminescence (PL) of CNF, TiCN/CNF, TiO₂/CNF and Pt-TiO₂/CNF were measured. The time profiles of photocurrent with electrodes of respective material are shown in Fig S6.[†] When the light is turned "on" the photocurrent is instantaneously produced, however when the

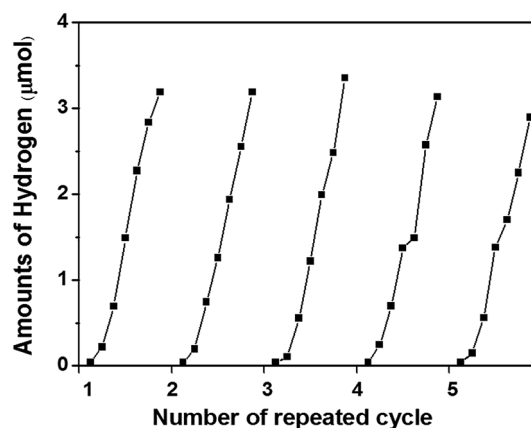


Fig. 8 Photocatalytic hydrogen generation using Pt(120)TiO₂/CNF spent sample under simulated solar light illumination after each interval of 3 hours.

light is turned “off”, the dark current is found to be negligible. It can be seen from the photocurrent profiles that the Pt–TiO₂/CNF sample shows the highest photocurrent value compared to other samples. The pure CNF shows negligible photocurrent, whereas the TiCN/CNF and TiO₂/CNF shows lower photocurrent than Pt–TiO₂/CNF. The synergistic photoresponse of Pt–TiO₂/CNF can be attributed to the presence of Pt on TiO₂ which increases the electron transfer and effectively suppress the e[−]–h⁺ recombination. The PL spectra for respective samples are also shown in Fig. S7.† The PL emission spectrum of pure TiO₂ (P25) was also measured as a reference. All the samples were excited at 325 nm and the PL spectra recorded in the range of 400–900 nm. The PL emission peak for TiO₂ (P 25) is centered around 500 nm. The enlarged view of PL emission peaks (because of weak intensity) for all the samples are shown in inset to Fig. S7.† The decrease in the intensity of PL emission peaks of samples follows the order: CNF, TiO₂/CNF, Pt–TiO₂/CNF and TiCN/CNF. It can be seen that the PL emission for Pt–TiO₂/CNF is decreased specifically in the range of 400–530 nm. This result indicates Pt photodeposition promotes the electron transfer from TiO₂/CNF to Pt and quenches the e[−]–h⁺ recombination.⁵⁶ While all the other PL emissions in the longer wavelength range (>530 nm) can be assigned to intrinsic defects and nonstoichiometry due to presence of oxygen vacancies in the mixed (anatase and rutile) phase TiO₂.^{57,58} The low intensity PL emission spectra of TiCN/CNF may be because of no or very low amount of mixed phase TiO₂ in the sample.

3.6. Photocatalytic stability test

The reusability and photocatalytic stability test of the Pt(*n*)–TiO₂/CNF sample was investigated by repeating the cycles of photocatalytic hydrogen generation with the same sample after a fixed time interval. The photocatalytic experiment was performed for five cycles as illustrated in Fig. 8. The illumination for each cycle was done for 30 minutes to study photocatalytic hydrogen yield. After the completion of first cycle the spent photocatalyst was recovered and the same sample was reused as a photocatalyst for the next four cycles. The spent photocatalyst was simply recovered by tweezers after each cycle, washed with DI water and reused. It is obvious from Fig. 8 that during all repeated cycles employing the same material, the recycling reactions produce approximately similar amount of hydrogen generation. These data confirm the photocatalytic stable performance of spent photocatalyst during all cycles of reaction and sufficiently support the reusability of the recovered photocatalyst.

4. Conclusions

In this work TiO₂ embedded CNF was prepared with the aim of achieving photocatalyst reusability and photocatalytically stable performance for photocatalytic hydrogen generation. The embedment of TiO₂ nanoparticles in PAN nanofibers was accomplished by electrospinning technique. The TiO₂/CNF was obtained by carbothermal reaction followed by calcination process. Formation of Pt–TiO₂/CNF was achieved by

photodeposition of platinum precursor on the TiO₂/CNF surface. The Pt photodeposition enhances the photocatalytic activity of the material due to increased electron transfer and reduced electron hole recombination. Furthermore we found that an increase in Pt photodeposition time results in an increase of photocatalytic hydrogen generation. However, we observed that the photocatalytic hydrogen generation becomes saturated with longer Pt photodeposition time (longer than 120 min). This saturation was due to excess deposition of Pt on the TiO₂/CNF, which cover the TiO₂ active sites and influence the photocatalytic performance of Pt–TiO₂/CNF.

The reusability and photocatalytic stability test of the prepared Pt–TiO₂/CNF was demonstrated by repeating the photocatalytic hydrogen generation cycles. The repetition was done after a fixed interval of time employing the same sample each time. Approximately similar amount of photocatalytic hydrogen was generated during each repeated cycle, assuring the stable behavior of Pt–TiO₂/CNF. On the basis of the characteristic physical properties of Pt–TiO₂/CNF, we believe that such a configuration will be advantageous and cost effective for large scale application in near future.

Acknowledgements

This work was supported by the DGIST R&D Program of the Ministry of Education, Science and Technology of Korea (14-NB-03 & 14-BD-0404). This research was supported by Basic Science Research Program through the National Research Foundation of Korea (NRF) funded by the Ministry of Science, ICT & Future Planning (2013R1A1A1008678).

References

- 1 S. Uemiyama, N. Sato, H. Ando, T. Matsuda and E. Kikuchi, *Appl. Catal., A*, 1991, **67**, 223–230.
- 2 S. J. Yoon, Y.-C. Choi and J.-G. Lee, *Energy Convers. Manage.*, 2010, **51**, 42–47.
- 3 K. Zeng and D. Zhang, *Prog. Energy Combust. Sci.*, 2010, **36**, 307–326.
- 4 M. Ni, M. K. H. Leung, D. Y. C. Leung and K. Sumathy, *Renewable Sustainable Energy Rev.*, 2007, **11**, 401–425.
- 5 A. Fujishima and K. Honda, *Nature*, 1972, **283**, 37–38.
- 6 A. Kudo and Y. Miseki, *Chem. Soc. Rev.*, 2009, **38**, 253–278.
- 7 K. Maeda and K. Domen, *J. Phys. Chem. Lett.*, 2010, **1**, 2655–2661.
- 8 X. Wang, G. Liu, Z.-G. Chen, F. Li, L. Wang, G. Q. Lu and H.-M. Cheng, *Chem. Commun.*, 2009, 3452–3454.
- 9 S. In, A. Orlov, F. Gracia, M. Tikhov, D. S. Wright and R. M. Lambert, *Chem. Commun.*, 2006, 4236–4238.
- 10 S. K. Parayil, H. S. Kibombo, C.-M. Wu, R. Peng, J. Baltrusaitis and R. T. Koodali, *Int. J. Hydrogen Energy*, 2012, **37**, 8257–8267.
- 11 H. J. Yun, H. Lee, N. D. Kim, D. M. Lee, S. Yu and J. Yi, *ACS Nano*, 2011, **5**, 4084–4090.
- 12 S. G. Lee, S. Lee and H.-I. Lee, *Appl. Catal., A*, 2001, **207**, 173–181.

- 13 N. Mandzy, E. Grulke and T. Druffel, *Powder Technol.*, 2005, **160**, 121–126.
- 14 M. Miyuuchi, A. Nakajima, T. Watanabe and K. Hashimoto, *Chem. Mater.*, 2002, **14**, 2812–2816.
- 15 S. K. Palaniswamy, S. Jayaraman, S. Subramanian, J. B. Veluru, S. Gurdev, I. A. Suleyman and R. Seeram, *Energy Environ. Sci.*, 2014, DOI: 10.1039/c4ee00612g.
- 16 S. Jayaraman, L. Ning, P. K. Suresh and R. Seeram, *Biofuel Research Journal*, 2014, **2**, 44–54.
- 17 V. J. Babu, M. K. Kumar, R. Murugan, M. M. Khin, R. P. Rao, A. S. Nair and S. Ramakrishna, *Int. J. Hydrogen Energy*, 2013, **38**, 4324–4333.
- 18 J. B. Varley, A. Janotti and C. G. V. d. Walle, *Adv. Mater.*, 2011, **23**, 2343–2347.
- 19 S. Chuangchote, J. Jitputti, T. Sagawa and S. Yoshikawa, *ACS Appl. Mater. Interfaces*, 2009, **1**, 1140–1143.
- 20 S. S. Lee, H. Bai, Z. Liu and D. D. Sun, *Appl. Catal., B*, 2013, **140**, 68–81.
- 21 W.-J. Fan, Z.-F. Zhou, W.-B. Xu, Z.-F. Shi, F.-M. Ren, H.-H. Ma and S.-W. Huang, *Int. J. Hydrogen Energy*, 2010, **35**, 6525–6530.
- 22 Y. Tong, X. Lu, W. Sun, G. Nie, L. Yang and C. Wang, *J. Power Sources*, 2014, **261**, 221–226.
- 23 A. Chinnappan and H. Kim, *Int. J. Hydrogen Energy*, 2012, **37**, 18851–18859.
- 24 B. Pant, N. A. M. Barakat, H. R. Pant, M. Park, P. S. Saud, J.-W. Kim and H.-Y. Kim, *J. Colloid Interface Sci.*, 2014, **434**, 159–166.
- 25 B. Pant, H. R. Pant, N. A. M. Barakat, M. Park, K. Jeon, Y. Choi and H.-Y. Kim, *Ceram. Int.*, 2013, **39**, 7029–7035.
- 26 S. Kim and S. K. Lim, *Appl. Catal., B*, 2008, **84**, 16–20.
- 27 M. Marella and M. Tomaselli, *Carbon*, 2006, **44**, 1404–1413.
- 28 A. Chambers, T. Nemes, N. M. Rodriguez and R. T. K. Baker, *J. Phys. Chem. B*, 1998, **102**, 2251–2258.
- 29 L.-F. Chen, X.-D. Zhang, H.-W. Liang, M. Kong, Q.-F. Guan, P. Chen, Z.-Y. Wu and S.-H. Yu, *ACS Nano*, 2012, **6**, 7092–7102.
- 30 H.-L. Kim, S. Kim, J.-K. Kang and W. Choi, *J. Catal.*, 2014, **309**, 49–57.
- 31 L. Zhang, J. Hu, A. A. Voevodin and H. Fong, *Nanoscale*, 2010, **2**, 1670–1673.
- 32 D. Li and Y. Xia, *Adv. Mater.*, 2004, **16**, 1151–1170.
- 33 Y. Yang, H. Wang, X. Lu, Y. Zhao, X. Li and C. Wang, *Mater. Sci. Eng., B*, 2007, **140**, 48–52.
- 34 S. A. C. Carabineiro, B. F. Machado, G. Dražić, R. R. Bacsá, P. Serp, J. L. Figueiredo and J. L. Faria, *Stud. Surf. Sci. Catal.*, 2010, 629–633.
- 35 H. T. Gomes, B. F. Machado, A. M. T. Silva, G. Dražić and J. L. Faria, *Mater. Lett.*, 2011, **65**, 966–969.
- 36 S. Aryal, C. K. Kim, K.-W. Kim, M. S. Khil and H. Y. Kim, *Mater. Sci. Eng., C*, 2008, **28**, 75–79.
- 37 N. Chandra, M. Sharma, D. K. Singh and S. S. Amritphale, *Mater. Lett.*, 2009, **63**, 1051–1053.
- 38 I.-J. Shon, B.-R. Kim, J.-M. Doh and J.-K. Yoon, *Ceram. Int.*, 2010, **36**, 1797–1803.
- 39 H. Lin, B. Tao, J. Xiong and Q. Li, *Int. J. Refract. Met. Hard Mater.*, 2013, **1**, 363–365.
- 40 X. Chen, Y. Li, J. Zhu, S. Jin, L. Zhao, Z. Lei and X. Hong, *Ceram. Int.*, 2008, **34**, 1253–1259.
- 41 L. M. Berger and W. Gruner, *Int. J. Refract. Met. Hard Mater.*, 2002, **20**, 235–251.
- 42 L. Di, Z. Xu, K. Wang and X. Zhang, *Catal. Today*, 2013, **211**, 109–113.
- 43 W. Y. Teoh, L. Mädler, D. Beydoun, S. E. Pratsinis and R. Amal, *Chem. Eng. Sci.*, 2005, **60**, 5852–5861.
- 44 S. K. Mohapatra, M. Misra, V. K. Mahajan and K. S. Raja, *J. Phys. Chem. C*, 2007, **111**, 8677–8685.
- 45 B. Luo, X. Yan, S. Xu and Q. Xue, *Electrochem. Commun.*, 2013, **30**, 71–74.
- 46 Y. Cong, X. Li, Y. Qin, Z. Dong, G. Yuan, Z. Cui and X. Lai, *Appl. Catal., B*, 2011, **107**, 128–134.
- 47 P. E. Restrepo, P. J. Arango and V. J. B. Palacio, *DYNA*, 2010, **77**, 64–74.
- 48 F. Sen and G. Gokkagac, *J. Phys. Chem. C*, 2007, **111**, 5715–5720.
- 49 K. Nishimiya, T. Hata, Y. Imamura and S. Ishihara, *J. Wood Sci.*, 1998, **44**, 56–61.
- 50 M. D. Driessen and V. H. Grassian, *J. Phys. Chem. B*, 1998, **102**, 1418–1423.
- 51 A. J. Bard, *J. Phys. Chem.*, 1982, **86**, 172.
- 52 K. Hashimoto, T. Kawai and T. J. Sakata, *J. Phys. Chem.*, 1984, **88**, 4083.
- 53 D. Eastman, *Phys. Rev. B: Solid State*, 1970, **2**, 1–2.
- 54 D. Tsukamoto, A. Shiro, Y. Shiraishi, Y. Sugano, S. Ichikawa, S. Tanaka and T. Hirai, *ACS Catal.*, 2012, **2**, 599–603.
- 55 W. Y. Park, G. H. Kim, J. Y. Seok, K. M. Kim, S. J. Song, M. H. Lee and C. S. Hwang, *Nanotechnology*, 2010, **21**, 195–201.
- 56 R. P. Antony, M. Tom, C. Ramesh, N. Murugesan, D. Arup, S. Dhara, S. Dash and A. K. Tyagi, *Int. J. Hydrogen Energy*, 2012, **37**, 8268–8276.
- 57 J. Shi, Z. Feng, T. Chen, Y. Lian, X. Wang and C. Li, *J. Phys. Chem. C*, 2007, **111**, 693–699.
- 58 H. Nakajima and T. Mori, *Phys. B*, 2006, **376–377**, 820–822.